

Spin-selectable, window-tunable negative differential resistance in graphene double ferromagnetic barriers

Yu Song,^{1,2,*} Yang Liu,^{1,2} Xiaolong Feng,^{1,2} Fei Yan,¹ and Wei-Zhi Zhang¹

¹*Institute of Electronic Engineering, China Academy of Engineering Physics, Mianyang 621999, P.R. China*

²*Microsystem & Terahertz Research Center, China Academy of Engineering Physics, Chengdu 610200, P.R. China*

(Dated: June 22, 2019)

We propose a spin-dependent negative differential resistance (NDR) device based on a short and wide graphene and two gated EuO strips deposited on top of it. We find clear significant of spin selectivity and window tunability in the spin-dependent NDR: by tuning the top gates, NDR for fermions of spin up only, spin down only, or both spins (occurring sequentially) can be realized respectively; meanwhile, the central position of NDR window in each case is monotonously tuned in a wide range of bias. These remarkable features are attributed to a gate controllability of the spin-dependent resonant levels in the device and their deviations from the Fermi energy and Dirac point in the source, respectively. They add a spin and a bias degrees of freedom to NDR-based devices, which paves a way for design of a whole new class of NDR circuits such as spin-selectable and output-tunable switching and spin memory.

I. INTRODUCTION

The intersection of spintronics and nonlinear transport can lead to phenomena of interest and use. For example, the realization of a spin-dependent negative differential resistance (NDR), in which one of the spins displays NDR while the other increases monotonically as the bias increases, can be applied as spin resolved oscillator [1], amplifier [2], switching [3], and memory [4]. Till now, several schemes have been proposed, based on graphene nanoribbons. For example, spin-dependent NDR have been demonstrated in edge-doped zigzag graphene nanoribbons (ZGNRs) [5–7], B(N)-doped ZGNRs [8], ZGNRs with nitrogen-vacancy defects [9], and zigzag-edged trigonal graphenes linked to ZGNRs electrodes [10]. In these devices spin-polarized edge states [11] play an important role. Other proposals considered armchair graphene nanoribbons (AGNRs), including FeN₄ embedded and N-doped AGNR [12] and a compound system comprising an AGNR and a set of ferromagnetic insulator strips deposited on top of it [13, 14]. However, till now none of the proposals has been experimentally implemented. This is partly because of the extreme difficulty in their fabrications, including careful tailors of the graphene edges and proper introduction of doping's, defects, or superlattices (SL).

In this work, we propose a bulk graphene based, spin-dependent double-barrier resonant tunneling diode (DB-RTD), which requires only depositing two gated EuO strips [15] on top of a wide and short graphene (see upper panel in Fig. 1). We find clear significant of spin-dependent resonant states in the device, which are demonstrated to dominate the biased transport when the Fermi energy is setting around them. As the bias increases the resonant levels shift to lower values, resulting in a decrease of the integration weights in the spin-

dependent current and a spin-dependent NDR. Furthermore, we find that, by changing the voltages of top gates hence the spin-dependent resonant levels, the spin index of the NDR can be tuned as spin up only, spin down only, or both spins. In each case, the central position of NDR window is monotonously tuned in a wide bias range. Together with the relative ease in fabrication, these remarkable features make the proposed device an important building block for future spin-selectable and output-tunable spintronic circuits.

Similar proposals have been presented recently. Lu et al. [16] and Zhang et al. [17] have studied a ferromagnetic SL and DB-RTD realized by depositing several magnetic insulators or two ferromagnetic stripes on top of graphene. They found a spin wavevector filtering and a spin beam splitter effect for a single electron. Dell et al [18] studied magnetic nanostructures made of an inhomogeneous perpendicular magnetic field and a ferromagnetic insulator. They found a spin filtering effect of linear conductance, but they did not study the effect of a finite bias, nor have they found NDR. Niu et al. [19] and Faizabadi et al. [20] (Zou et al [21]) have investigated a ferromagnetic SL (DB RTD) made of gated magnetic insulators on top of graphene. They found a spin polarization of tunneling conductance and an oscillatory behavior of the tunneling magnetoresistance as a function of the gate voltage, but they did not consider the finite bias either.

On the other hand, in their calculations all these works [13–16, 18–21] adopted a simple Zeeman splitting model to describe the magnetic proximity effect. This model is roughly estimated from the analogy with a EuO/Al interface [15] and considers only opposite energy shifts for opposite spins added to the linear dispersion of a pristine graphene. Since 2012, the magnetic proximity effect have been experimentally realized, for example, by depositing EuO [22] or EuS [23] on graphene, or by transferring graphene onto yttrium iron garnet [24–27] or La_{0.7}Sr_{0.3}MnO₃ [28]. Interestingly, heavy electron dop-

* Corresponding author; kwungyusung@gmail.com

ing's and finite Dirac gaps are found [22–24]. Ab-initio calculations [29, 30] further demonstrate large spin Dirac gaps accompany with parabolic dispersions. Others [30–32] and we [33, 34] have developed effective Hamiltonians in a sublattice-spin direct product space or a sublattice space, based on which nontrivial effects, such as quantum anomalous Hall effect [32], simultaneous spin filter and spin valve effect [33], electric-field-induced colossal magnetoresistance [34], and pure crossed Andreev reflection [35] have been explored.

In this work, we investigate the spin-dependent currents at finite bias in the proposed device by using the ab-initio electronic structure. The structure of the paper is as follows. In Sec. II we present the setup of the device and the formula to calculate the stationary envelop function as well as the transmission coefficient for a given spin, energy, incident angle, and bias voltage across the sample. The ab-initio dispersions and a linear voltage drop are considered. The resulting current-voltage characteristics of the device, comprising a spin-dependent NDR with selectable spin and tunable window, and a spin current filter effect are discussed in the subsequent Sec. III. The mechanism for the arising and tunability of the spin-dependent NDR, as well as possible applications of its remarkable features are emphasized. Finally, Sec. IV concludes the paper.

II. SETUP AND FORMULA

The proposed system is composed of a sufficiently wide ($W=250$ nm) and short rectangular graphene and two rectangular strips of EuO on top of it (see the upper panel of Fig. 1). The length of the strips is $a = 21.75$ nm and the spacing between them is $b = 8.7$ nm. Buffer regions between the EuO and electrodes are set as $a/10$. The total length $l = 2.2a + b$ is several times smaller than W , hence the transport is dominated by bulk states [36] and no specific control of the edge type is needed. On top of the EuO strips two top gates ($V_t^{(i)}, i = 1, 2$) are applied. They are used to tune the local carrier concentrations and lift the Dirac points of the two ferromagnetic graphene's ($E_D = -1.37$ eV [29]) to align with that of the pristine graphene, see the middle panel of Fig. 1. In this case, spin-dependent barriers can be used. Below the substrate a back gate (V_g) is applied to tune the Fermi energy (E_F) through the whole sample. Therefore, a spin-up and spin-down electron propagating along the sample will be subjected to two different rectangular barriers. In other words, the array of two gated EuO strips creates a spin-dependent DB-RTD. The source and drain electrodes may induce a charge doping (U).

When a bias voltage (V_b) is applied between the source and drain, a net current will be produced. The current is contributed by the electrons or holes in the source within an energy range of $(E_F - V_b, E_F)$ at zero-temperature, see the bottom panel in Fig. 1. Due to the spin difference in the ferromagnetic regions, the current will be

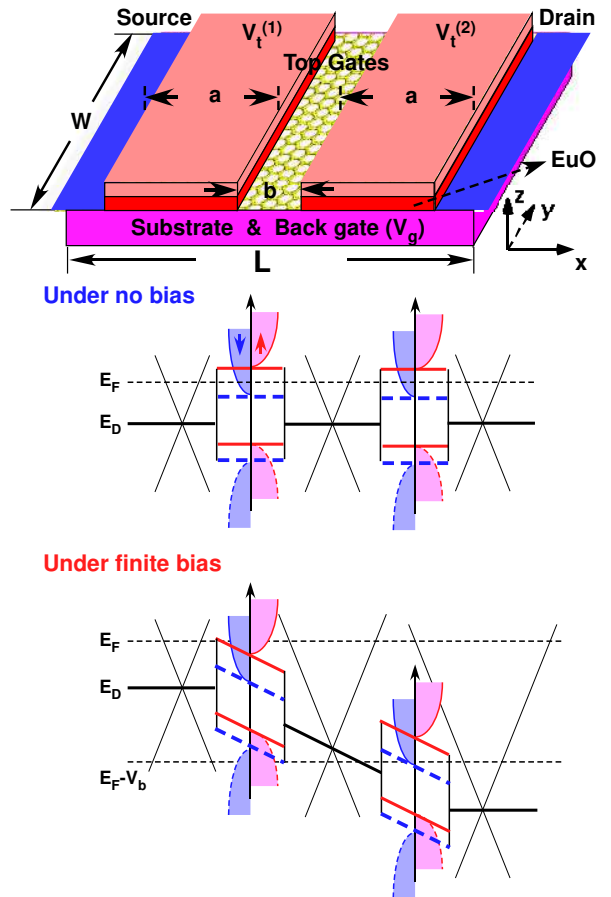


FIG. 1. Schematic diagrams of the proposed device (upper panel) and the voltage profiles under zero (middle panel) or finite (bottom panel) biases.

spin resolved. Unlike other works concerning NDR in graphene which consider a step-like voltage drop, in this work we also consider a linear voltage drop, $V(x) = fx$ with $f = V_b/l$, between the source and drain along the x -direction.

As we have indicated, the proximity-induced ferromagnetism in graphene can be viewed as spin-resolved Dirac cone doping's (D_s), spin-resolved Dirac gaps (Δ_s), and spin-resolved Fermi velocity v_s ($s = \pm 1$ for spin up and down) [33, 34]. Accordingly, the dispersions can be described by an effective Hamiltonian in a sublattice space [33, 34, 37]

$$\mathcal{H}_{\mathbf{k},s,\xi}^f = \boldsymbol{\sigma} \cdot \hbar v_s \mathbf{k} + \xi \sigma_z \Delta_s + \mathcal{I}(D_s + V_t^{(i)} + V(x)). \quad (1a)$$

Here $\boldsymbol{\sigma} = (\sigma_x, \sigma_y)$ is a pseudospin Pauli matrices, $\mathbf{k} = (k_x, k_y)$ is a momentum operator, $\xi = \pm 1$ is an index for valley K and K' , and \mathcal{I} is an identity matrix. We consider graphene on six bi-layer EuO, for which the parameters read $D_{+(-)} = 42$ (-24) meV, $\Delta_{+(-)} = 134$ (98) meV, and $v_{+(-)} = 1.337$ (1.628) v_F , respectively [29, 33]. For the pristine graphene in the buffer regions or between the

ferromagnetic ones, the Hamiltonian is well known

$$\mathcal{H}_{\mathbf{k}}^p = \boldsymbol{\sigma} \cdot \hbar v_F \mathbf{k} + \mathcal{I}V(x). \quad (1b)$$

For the contacted graphene in the source and drain, the Hamiltonian reads

$$\mathcal{H}_{\mathbf{k}}^c = \boldsymbol{\sigma} \cdot \hbar v_F \mathbf{k} + \mathcal{I}U. \quad (1c)$$

For convenience, we express all physical quantities in their dimensionless form in terms of a characteristic length $l_0 = 56.55\text{nm}$ and a corresponding energy unit $E_0 = \hbar v_F/l_0 = 10\text{meV}$. Under this condition the charge density of states is coinciding with a true system and a coherent transport regime is ensured even at room temperature. The transverse momentum $k_y = (E-U) \sin \alpha$ (α is the incident angle) together with the wave function $e^{ik_y y}$ is conserved, and it suffices to solve for the longitudinal wave function $\Psi_j(x)$, where $j = c, f, p$ for the contacted, ferromagnetic, and pristine graphene, respectively. However, straightforward decoupling of $\mathcal{H}_j \Psi_j(x) = E \Psi_j(x)$ in Eqs. (1a) and (1b), which contain a linear term of x , results in an unsolvable two-order differential equation [38]. To solve this problem, we perform a rotation of the Dirac equation by $\pi/2$ around the y -axis in the pseudospin space (see the upper panel of Fig. 1). The envelope functions become resolvable and the result for the ferromagnetic graphene reads

$$\Psi_f^s = f^+ \begin{pmatrix} F_s(x) \\ G_s^*(x) \end{pmatrix} e^{ik_y y} + f^- \begin{pmatrix} G_s(x) \\ F_s^*(x) \end{pmatrix} e^{ik_y y}, \quad (2a)$$

where $F_s(x) = D[-1/2 + iq_s^2/2a_s, (1+i)(E - D_s - V_t^{(i)} + fx)/\sqrt{a_s}]$ and $G_s(x) = D[-1/2 - iq_s^2/2a_s, (-1+i)(E - D_s - V_t^{(i)} + fx)/\sqrt{a_s}]$ with D being the Weber parabolic cylinder function, $q_s^2 = \Delta_s^2 + k_y^2$, and $a_s = f v_s$. Note, $F_s(x)$ and $G_s^*(x)$ ($F_s^*(x)$ and $G_s(x)$) are spin resolved and have properties of a right (left)-going wave function [38]. For the pristine graphene the result becomes

$$\Psi_p = p^+ \begin{pmatrix} F(x) \\ G^*(x) \end{pmatrix} e^{ik_y y} + p^- \begin{pmatrix} G(x) \\ F^*(x) \end{pmatrix} e^{ik_y y}, \quad (2b)$$

where $F = D[-1/2 + ik_y^2/2f, (1+i)(E + fx)/\sqrt{f}]$ and $G = D[-1/2 - ik_y^2/2f, (-1+i)(E + fx)/\sqrt{f}]$. In the rotated pseudospin space, the envelope functions for the contacted graphene become

$$\Phi_c^\pm = c^\pm \begin{pmatrix} 1 \pm e^{\pm i\alpha} \\ -1 \pm e^{\pm i\alpha} \end{pmatrix} e^{\pm ik_c x + ik_y y}, \quad (2c)$$

where $k_c^{s,d} = \text{Sign}[E - U + V_b^{s,d}] \sqrt{(E - U + V_b^{s,d})^2 - k_y^2}$ with $V_b^{s,d} = 0, V_b$. In the source, $c^+ = 1$ and $c^- = r_s$ (the spin-resolved reflection coefficients), while in the drain $c^+ = t_s$ (the spin-resolved transmission coefficients) and $c^- = 0$.

With the standard transfer-matrix method [39] t_s can be obtained by matching the spinor envelope functions in Eq. (2) at the potential boundaries ($x =$

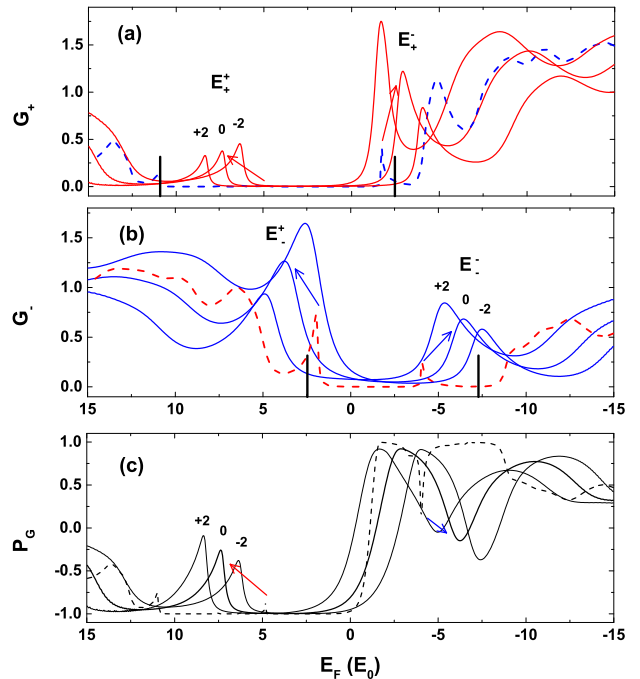


FIG. 2. (a,b) Linear conductances for spin up (a) and spin down (b) as a function of the Fermi energy. Dashed: $l = 2$ and $V_t^{(i)} = 0$, solid: $l = 1$ and $V_t^{(i)} = -2, 0, 2$. (c) The corresponding spin polarizations.

$0, 0.1a, 1.1a, 1.1a + b, 2.1a + b, l$). The transmission probability reads

$$T_s(E, \alpha, V_b) = |t_s|^2 \frac{k_c^d}{E - U + V_b} \left(\frac{k_c^s}{E - U} \right)^{-1} \quad (3)$$

for $(k_c^s)^2 > 0$ and $(k_c^d)^2 > 0$, and $T_s = 0$ otherwise. The spin-resolved net current at zero temperature can be calculated by the Landauer-Büttiker formalism [40]

$$I_s(E_F, V_b) = I_0 \int_{E_F - V_b}^{E_F} \int_{-\pi/2}^{\pi/2} T_s |E| \cos \alpha d\alpha dE, \quad (4)$$

where $I_0 = 2ev_F W / (2\pi l_0)^2$ is a current unit with the factor 2 coming from the valley degeneracy. $(E_F - V_b, E_F)$ is the integrated window. $\int_{-\pi/2}^{\pi/2} T_s \cos \alpha d\alpha = G_s$ can be regarded as a spin-dependent differential conductance; it has an integrated weight of $|E|$. Considering the values of W and l_0 , $I_0 = 60\mu\text{A}$, which is one or two orders of magnitudes larger than those in graphene nanoribbons [5–13]. The total current and spin polarization are defined as $I = I_+ + I_-$ and $P_I = (I_+ - I_-) / I \times 100\%$.

III. RESULTS AND DISCUSSION

A. Spin conductance at zero bias

Figure 2 (a,b) shows the spin-dependent linear conductance through the unbiased sample as a function of the

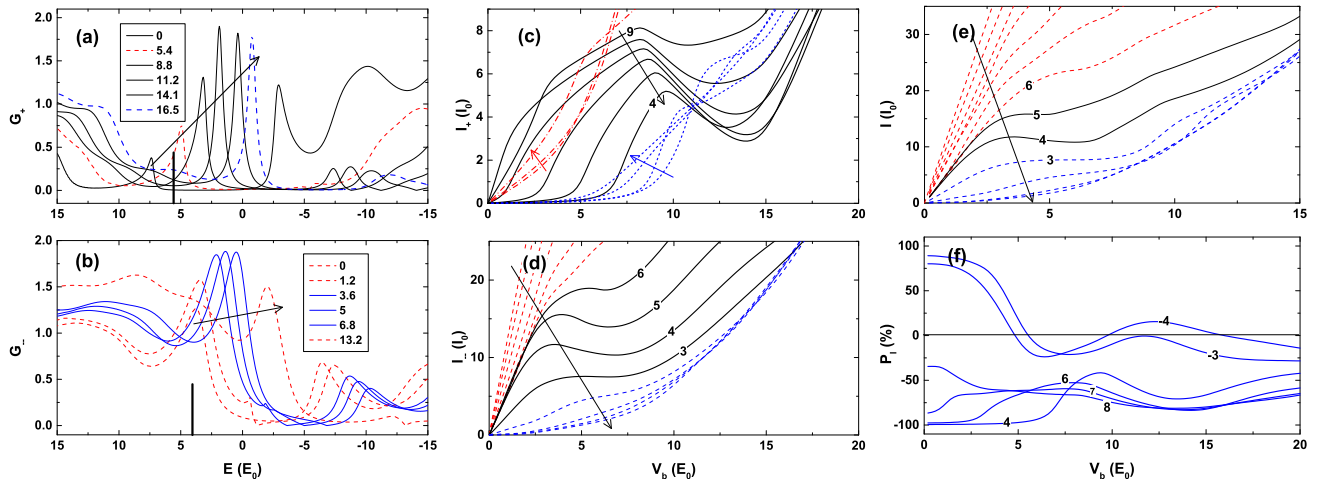


FIG. 3. (a, b) Spin-dependent differential conductance as a function of the energy for several typical biases. (c, d) I-V characteristics at various Fermi energies with a step of 1 for spin up and spin down. (e, f) Total current and its spin polarization as a function of the bias for various Fermi energies indicated in the figure.

Fermi energy. The calculations can be made by following Ref. [34]. It is seen that, already for a relatively short length ($l = 2$ with $a = 43.5$ nm and $b = 17.4$ nm, dashed), the spin linear conductance shows a good accordance to the spin band gaps, for which the conduction band minimum (CBM) and valence band maximum (VBM) are indicated by the vertical bars. Inside each spin Dirac gap two resonant peaks (E_+^\pm and E_-^\pm , as indicated in the figure) arise. This is a clear significant of resonant tunneling. For a shorter device ($l = 1$, solid) the resonant peaks shift outside and become stronger (indicated by the arrows). Compare with spin up, the resonant tunneling is much weaker for spin down. This is a result of a smaller effective spin Dirac gap, i.e., $\Delta_{\text{eff}}^- = \frac{\Delta_-}{v_-} \approx 6 < \Delta_{\text{eff}}^+ = \frac{\Delta_+}{v_+} \approx 10$ [34]. The spin-dependent linear conductance at different top gates are also shown. It is seen that, the spin resonant energy becomes larger (smaller) as a positive (negative) top gate is applied.

The total conductance is spin dependent, which manifests itself clearly in the polarization, defined as $P_G = (G_+ - G_-)/(G_+ + G_-) \times 100\%$. Near-full polarizations of opposite signs can be found in the ranges between CBMs (VBMs) of different spins, i.e., the electron (hole) splitting window. They are much higher than spin polarizations obtained in Refs. [18, 21] and can be used as a spin conductance filtering. On the other hand, the spin filtering effect is found to be weakened by the resonant tunneling and can be exactly controlled by the top gates.

B. Spin-dependent NDR

The spin-dependent currents as a function of bias are plotted in Fig. 3(c,d). Here various Fermi energies are considered. In Fig. 3(c) it is seen that, for Fermi ener-

gies around the positive resonant level $E_+^+ = 7.37$ (black solid), the spin up current displays obvious NDR. However, for Fermi energy much higher (> 9 , red dashed) or smaller (< 3.5 , blue dashed) than the resonant energy, the NDR features disappear.

To understand these behaviors, we plot the spin up differential conductance as a function of energy under different biases in Fig. 3(a). It is seen that, for Fermi energies around the resonant level, the transport under bias is dominated by the resonant state. Considering several typical biases in the strongest NDR case ($E_F = 5.5$). As the bias increases from zero (the $V_b = 5.4$ line), the resonant peak shifts into the integrated window with an increasing peak value. This leads to an increase behavior of the spin-dependent current with an increasing bias. The spin up current reaches its maximum at a bias of $V_P = 8.8$, where the resonant state has totally inserted into the integration window. It is seen from Eq. (4)

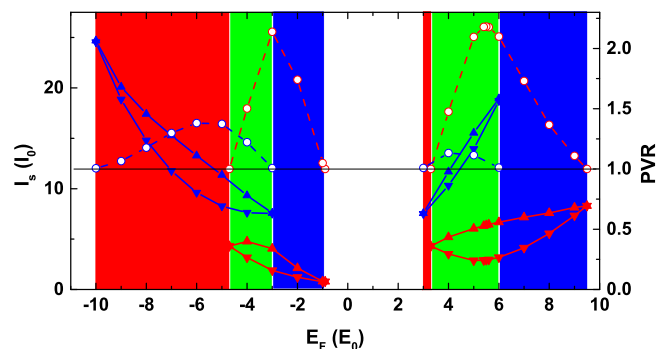


FIG. 4. Peak and valley currents (solid) and their ratio (dashed) as a function of the Fermi energy. Red for spin up and blue for spin down. In the red, green, and blue windows, NDR happens for spin down only, both spins, and spin up only, respectively.

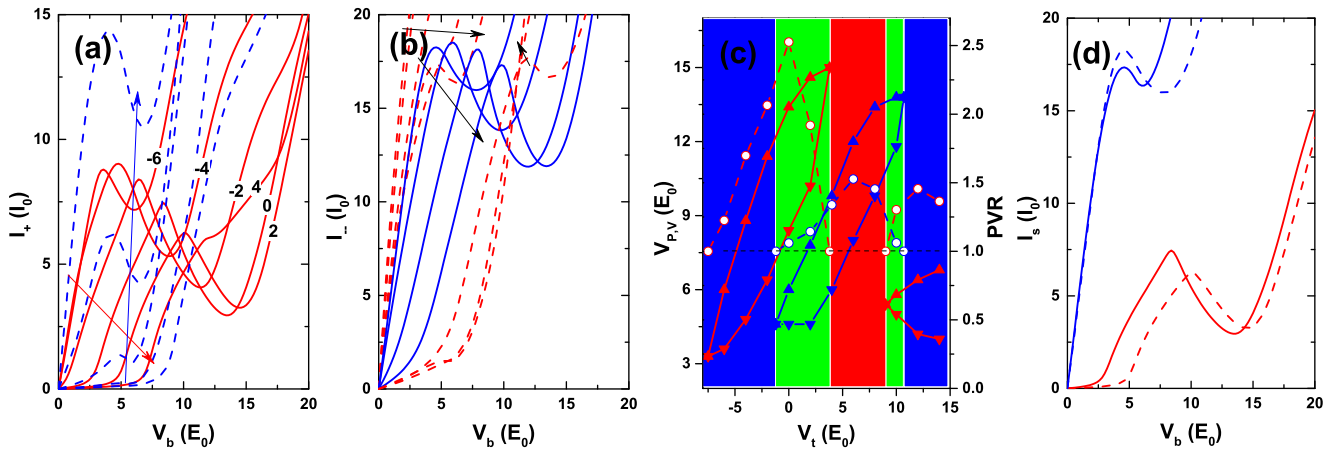


FIG. 5. (a, b) Spin-dependent I-V characteristics for $E_F = 5.5$ and various top gates. In (a) the top gates increase from -6 to 4 (6 to 14) with a step of 2 along the red (blue) arrow; In (b) the top gates increase from -6 to 0, 2 to 8, and 10 to 14 with a step of 2, respectively. (c) The bias voltages for the current peak and valley (solid) and the PVR (dashed) as a function of the top gates, red for spin up and blue for spin down. (d) Dual-spin NDR at top gates of 0 and 2.

that, the spin-dependent resonant states contribute to the spin-dependent currents by a weight of an absolute value of its energy $|E|$, which is similar to a density of state. As the bias increases further (the $V_b = 11.2$ line), the weight decreases and results a decrease behavior of the spin up current with an increasing bias, i.e., the NDR feature. The weight decreases because as the bias increases the positive resonant level shifts down closed to the Dirac point in the source ($|E| = E$ becomes smaller). The current achieves its minimum at a larger bias ($V_b = 14.1$), where the dropping resonant level almost aligns to the Dirac point of the source and the weight approaches almost zero. However, as the bias increases further (the $V_b = 16.5$ line), the shift down of a negative resonant level leads to an increase of the weight ($|E| = -E$ becomes bigger). As a result, the spin up current increases again.

For Fermi energies far from the resonant level, the biased transport is also contributed by quasi-ballistic state outside the spin Dirac gap, see Fig. 3(a). As a result, the bias-induced decrease of the weight is counteracted by the bias-induced increase of the integrating window, and the NDR feature disappears. For spin down, much less pronounced NDR are found for different Fermi energies around $E_F^+ = 3.77$ (see Fig. 3(d)). This stems from a more expanding resonant peak, which is shown in Fig. 3(b), where several typical bias for the strongest NDR ($E_F = 4.0$) case is considered.

For each spin, the peak and valley currents at V_P and V_V as well as their ratios as a function of Fermi energy are plotted in Fig. 4. From the figure, the spin dependence of the NDR becomes more clear. Obvious NDR features are also found for spin up around $E_F^+ = -2.93$ and for spin down around $E_F^- = -6.43$. It is seen that, according to the occur of spin-dependent NDR only around the corresponding resonant level, the peak-to-valley ratio (PVR) shows a non-monotonous dependence on the

Fermi energy, from 1 (no NDR) to certain value and to 1 again. The maximum PVR for a spin is found at a Fermi energy slightly higher than the corresponding resonant level. For spin up, the value reads 2.2, which is comparable with those obtained in experiments on spin-independent NDRs [41, 42]. On the other hand, it is also seen that, around the positive and negative resonant levels the peak and valley currents show opposite dependence on E_F .

More importantly, although the spin up and spin down NDRs happen at different Fermi energies around different resonant levels, NDRs for both spins can be realized for certain Fermi energy between E_F^+ and E_F^- (or between E_F^- and E_F^+), see the green windows in Fig. 4. This is also clear in Fig. 3(c,d), in which the $E_F = 4, 5, 6$ cases show NDR for both spins. In Fig. 3(c,d), it is also observed that the NDR windows for different spins do not overlap. As a result, the proposed device can be applied as a *dual spin Esaki diode*: at low bias spin down displays NDR and at high bias spin up displays NDR. In another view, this remarkable behavior adds spin degree of freedom to multiple separate NDR regions. For Fermi energy higher (lower) than this region, see the blue (red) windows, only spin up (spin down) shows NDR while the other spin increases monotonously with the bias. This can be applied as a *single spin Esaki diode*. Hence, spin-dependent NDR with selectable spin can be realized in the proposed device by simply tuning the back gate.

C. Spin current filtering at finite bias

We further address the total current I through the device, as well as its spin polarization P_I . Figs. 3 (e) and 3(f) show that the total current displays a clear linear behavior for high Fermi energies, which transfers to a resonant behavior at moderate Fermi energies and an

exponential behavior at low Fermi energies. The latter can be applied as a normal diode whose behavior is described by the Shockley diode equation. The resonant behavior is a superposition of the spin-dependent NDRs. However, for the total current the NDR happens only for $3 < E_F < 6$, which is narrower than the right green window in Fig. 4. This stems from that the dominate spin (spin down) displays a strong NDR and can be applied as a normal Esaki diode.

It can be seen in Fig. 3(f) that, for Fermi energies lying in the electron or hole splitting window, the current polarization at low bias is close to -100% or 100% . This is in good accordance to Fig. 2. However, the high polarization decreases sharply with an increasing bias, which implies that for these Fermi energies the device can only operate as a spin *conductance* filter. Remarkably, for Fermi energies lying in the right blue window in Fig. 4, high polarization ($\sim -80\%$) can be obtained even at a rather high bias ($V_b \sim 14$). This is a spin *current* filtering effect, which is different from the spin conductance filtering effect at zero bias as discussed in Sec. III A and other works [18–21]. Nonmonotonous behavior of the polarization is also observed. Interestingly, for Fermi energy around -4 , zero polarization can be obtained at a high bias.

D. Top-gates control of the spin NDRs

We further consider spin-dependent I-V characteristics at various top gates, which is shown in Fig. 5(a,b). The spin-dependent NDR windows, (V_P^+, V_V^+) and (V_P^-, V_V^-) , as well as PVRs are summarized in Fig. 5(c). From the five windows in Figs. 5 (c) we can see that, as the top gates increases from -7 to 15 , the device works consecutively as a spin-up only, dual-spin, spin-down only, dual-spin, and spin-up only Esaki diode, which is similar to that happens under increasing Fermi energies (see Fig. 4). The PVR show a non-monotonic dependence on the top gates, similar to that on the Fermi energy. We also find that, a certain asymmetry of the barriers ($\Delta V_t = V_t^{(1)} - V_t^{(2)} < 0$) can enhance the PVR. For $\Delta V_t = -2$ the value changes from 2.18 to 2.52 .

Remarkably, when the top gates increase from -7 to -1.2 (the first window in Fig. 5 (c)), the spin up NDR window shifts monotonously to a higher bias. The lowest window centers at ~ 3 and the highest window centers at ~ 9 . In other words, by tuning the top gates in this range the operation window of the spin-up Esaki diode can change in a wide range of $\sim 60\text{meV}$. When $V_t^{(i)}$ further increase from -1.2 to 3.8 (the second window in Fig. 5 (c)), both the spin up and spin down NDR windows shift monotonously to a higher bias. This means that the two operation windows of the dual-spin Esaki diode can be exactly controlled. The tunable ranges for spin up and spin down are $\sim 60\text{ meV}$ and $\sim 30\text{ meV}$, respectively. For top gates between 3.8 and 9 , the operation window of the spin-down Esaki diode can be monotonously tuned

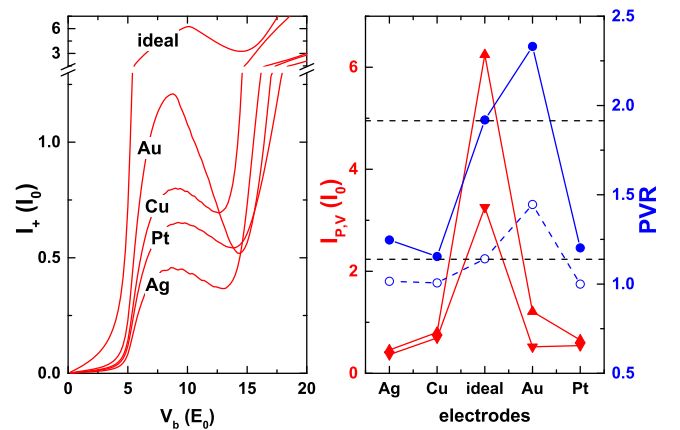


FIG. 6. (a) Spin up I-V characteristics at different electrode contacting. (b) Peak and valley currents (red solid) and PVR (blue solid) for spin up, and PVR for spin down (blue dashed) at different contacting.

by $\sim 70\text{ meV}$.

The spin selectivity and window tunability of the spin-dependent NDR can be understood as follows. As the top gates increase, the spin-dependent resonant levels formed between the two barriers are lift, and E_+^+ , E_-^+ , E_-^- , and E_+^- are consecutively closed to the fixed Fermi energy hence made use of, solely or simultaneously. The former leads to a single spin Esaki diode while the latter results in a dual spin Esaki diode. On the other hand, for each resonant level made use of, its distance to the Dirac point in the source enlarges with the increasing top gates, see Fig. 2(a,b). As a result, the decrease of the integration weight hence the spin-dependent NDR will happen at a higher bias. In Fig. 3 the spin-dependent NDR window is also found to be controlled by the Fermi energy. However, the change is non monotonous.

Spin oscillator, spin amplifier, spin switching, and spin memory can be realized based on a spin-dependent NDR. The gate-induced spin selectivity in the proposed device adds a spin degree of freedom to these devices: by simply tuning the top gates as low, high, and medium values, spin devices for spin up only, for spin down only, or for both spins occurring sequentially can be respectively realized. On the other hand, the window tunability in the proposed device further adds an output degree of freedom to these spin devices, especially in spin switching and spin memory, whose lowest output voltage and two stored states are found to be exactly determined by the bias position of the NDR window (see Ref. [43] and relevant references therein).

E. Electrode doping effect

In all the above calculations, the effect of the electrode dopings is ignored. Such an ideal contact can be achieved by specific metals with special distance to graphene (e.g.,

Au/Cu/Ag at 3.2/3.4/3.7Å) [44]. However, for familiar metal electrodes such as Ag, Cu, Au, and Pt at their equilibrium distances, the contact doping are $U/E_0 \sim -32, -17, 19,$ and $32,$ respectively [44], which are comparable with the spin Dirac gap in ferromagnetic graphene ($\Delta_{+(-)} = 13.4(9.8)E_0$) [34]. Hence it is important to investigate how the spin-dependent NDR can be affected by the contact doping. In Fig. 6(a) we plot the calculated spin up I-V characteristic. It is seen that, the spin-dependent current decreases as the contact becomes non-ideal; the heavier the doping, the stronger the decrease. In surprise, the PVR can be enhanced for some positive contacting doping, e.g., Cu, see Fig. 6(b), where $I_P, I_V,$ and the PVR are plotted. For spin up, the PVR is enhanced from 1.92 at ideal contact to 2.33 at Cu contact, with an enhancement factor of 21%; while for spin down the change is from 1.14 to 1.45, with an enhancement factor of 27%. Other metals with positive contact doping smaller than ~ 240 meV can also be used to obtain a larger PVR than the ideal contact case.

IV. CONCLUSION

In summary, we have proposed a bulk graphene based, spin-dependent NDR device, which is comprising a short and wide graphene and two gated EuO strips deposited

on top of it. The spin-dependent NDR arises because the energies (integration weights) of the spin-dependent resonant states decrease with an increasing bias. Compared with spin-dependent NDR devices based on zigzag or armchair GNRs, the proposed device holds the advantages of no need of edge tailor, generation of larger currents, and most importantly, features of spin selectivity and window tunability induced by top gates. These remarkable features stem from a top-gate control of the deviations between the spin-dependent resonant levels and the Fermi energy (Dirac point) in the source. They add a spin and a bias degree of freedom to NDR-based devices, which paves a way for design of a whole new class of NDR circuits such as spin-selectable and output-tunable switching and memory.

The proposed device can also be applied as a spin current filter at high bias.

ACKNOWLEDGEMENTS

This work was supported by the National Natural Science Foundation of China (NSFC) under Grant No. 11404300, the Science Challenge Project (SCP) under Grant No. TZ2016003-1, and the S&T Innovation Fund of IEE, CAEP under Grant No. S20140807.

-
- [1] E. Alekseev and D. Pavlidis, *Solid State Electron* **44**, 941 (2000).
 - [2] J. Laskar, A. Ketterson, J. Baillargeon, T. Brock, I. Adesida, K. Cheng, and J. Kolodzey, *IEEE Electron Device Lett.* **10**, 528 (1989).
 - [3] W.-C. Liu, J.-H. Tsai, W.-S. Lour, L.-W. Lai, S.-Y. Cheng, K.-B. Thei, and C.-Z. Wu, *IEEE Trans. Electron Devices* **44**, 520 (1997).
 - [4] J. Van Der Wagt, *Proc. IEEE* **87**, 571 (1999).
 - [5] T.-T. Wu, X.-F. Wang, M.-X. Zhai, H. Liu, L. Zhou, and Y.-J. Jiang, *Appl. Phys. Lett.* **100**, 052112 (2012).
 - [6] C. Jiang, X.-F. Wang, and M.-X. Zhai, *Carbon* **68**, 406 (2014).
 - [7] S.-L. Yan, M.-Q. Long, X.-J. Zhang, and H. Xu, *Phys. Lett. A* **378**, 960 (2014).
 - [8] X.-F. Yang, W.-Q. Zhou, X.-K. Hong, Y.-S. Liu, X.-F. Wang, and J.-F. Feng, *J. Chem. Phys.* **142**, 024706 (2015).
 - [9] T. Xu, J. Huang, and Q.-x. Li, *Chinese J. Chem. Phys.* **27**, 653 (2014).
 - [10] X. Hong, Y. Kuang, C. Qian, Y. Tao, H. Yu, D. Zhang, Y.-S. Liu, J. Feng, X. Yang, and X.-F. Wang, *J. Phys. Chem. C* **120**, 668 (2015).
 - [11] Y. Son, M. Cohen, and S. Louie, *Nature* **444**, 347 (2006).
 - [12] N. Liu, J. Liu, K. Yao, Y. Ni, and S. Wang, *J. Appl. Phys.* **119**, 104301 (2016).
 - [13] J. Munárriz, C. Gaul, A. V. Malyshev, P. Orellana, C. A. Müller, and F. Domínguez-Adame, *Phys. Rev. B* **88**, 155423 (2013).
 - [14] E. Díaz, K. Miralles, F. Domínguez-Adame, and C. Gaul, *Appl. Phys. Lett.* **105**, 103109 (2014).
 - [15] H. Haugen, D. Huertas-Hernando, and A. Brataas, *Phys. Rev. B* **77**, 115406 (2008).
 - [16] W.-T. Lu, W. Li, Y.-L. Wang, H. Jiang, and C.-T. Xu, *Appl. Phys. Lett.* **103**, 062108 (2013).
 - [17] Q. Zhang and K. Chan, *Appl. Phys. Lett.* **105**, 212408 (2014).
 - [18] L. DellAnna and A. De Martino, *Phys. Rev. B* **80**, 155416 (2009).
 - [19] Z. Niu, F. Li, B. Wang, L. Sheng, and D. Xing, *Eur. Phys. J. B.* **66**, 245 (2008).
 - [20] E. Faizabadi, M. Esmailzadeh, and F. Sattari, *Eur. Phys. J. B.* **85**, 1 (2012).
 - [21] J. Zou, G. Jin, and Y.-q. Ma, *J. Phys. Condens. Matter* **21**, 126001 (2009).
 - [22] A. G. Swartz, P. M. Odenthal, Y. Hao, R. S. Ruoff, and R. K. Kawakami, *ACS Nano* **6**, 10063 (2012).
 - [23] P. Wei, S. Lee, F. Lemaitre, L. Pinel, D. Cutaia, W. Cha, F. Katmis, Y. Zhu, D. Heiman, J. Hone, *et al.*, *Nature Mater.* **15**, 711 (2016).
 - [24] Z. Wang, C. Tang, R. Sachs, Y. Barlas, and J. Shi, *Phys. Rev. Lett.* **114**, 016603 (2015).
 - [25] J. Mendes, O. A. Santos, L. Meireles, R. Lacerda, L. Vilela-Leão, F. Machado, R. Rodríguez-Suárez, A. Azevedo, and S. Rezende, *Phys. Rev. Lett.* **115**, 226601 (2015).
 - [26] J. C. Leutenantsmeyer, A. A. Kaverzin, M. Wojtaszek, and B. J. van Wees, *2D Mater.* **4**, 014001 (2016).

- [27] M. Evelt, H. Ochoa, O. Dzyapko, V. E. Demidov, A. Yurgens, J. Sun, Y. Tserkovnyak, V. Bessonov, A. B. Rinkevich, and S. O. Demokritov, *Phys. Rev. B* **95**, 024408 (2017).
- [28] S. Sakai, S. Majumdar, Z. I. Popov, P. V. Avramov, S. Entani, Y. Hasegawa, Y. Yamada, H. Huhtinen, H. Naramoto, P. B. Sorokin, *et al.*, *ACS Nano* **10**, 7532 (2016).
- [29] H.-X. Yang, A. Hallal, D. Terrade, X. Waintal, S. Roche, and M. Chshiev, *Phys. Rev. Lett.* **110**, 046603 (2013).
- [30] A. Hallal, F. Ibrahim, H. Yang, S. Roche, and M. Chshiev, *2D Mater.* **4**, 025074 (2017).
- [31] K. Zollner, M. Gmitra, T. Frank, and J. Fabian, *Phys. Rev. B* **94**, 155441 (2016).
- [32] S. Su, Y. Barlas, J. Li, J. Shi, and R. K. Lake, *Phys. Rev. B* **95**, 075418 (2017).
- [33] Y. Song and G. Dai, *Appl. Phys. Lett.* **106**, 223104 (2015).
- [34] Y. Song, arXiv:1708.01858 (2017).
- [35] Y. S. Ang, L. Ang, C. Zhang, and Z. Ma, *Phys. Rev. B* **93**, 041422 (2016).
- [36] J. Tworzydło, B. Trauzettel, M. Titov, A. Rycerz, and C. W. Beenakker, *Phys. Rev. Lett.* **96**, 246802 (2006).
- [37] C. Beenakker, *Rev. Mod. Phys.* **80**, 1337 (2008).
- [38] E. Sonin, *Phys. Rev. B* **79**, 195438 (2009).
- [39] M. Born and E. Wolf, *Principles of optics: electromagnetic theory of propagation, interference and diffraction of light* (Elsevier, 2013).
- [40] M. Büttiker, Y. Imry, R. Landauer, and S. Pinhas, *Phys. Rev. B* **31**, 6207 (1985).
- [41] L. Britnell, R. Gorbachev, A. Geim, L. Ponomarenko, A. Mishchenko, M. Greenaway, T. Fromhold, K. Novoselov, and L. Eaves, *Nat. Commun.* **4**, 1794 (2013).
- [42] P. Sharma, L. S. Bernard, A. Bazigos, A. Magrez, and A. M. Ionescu, *ACS Nano* **9**, 620 (2015).
- [43] H. Mizuta and T. Tanoue, *The physics and applications of resonant tunnelling diodes*, Vol. 2 (Cambridge University Press, 2006).
- [44] G. Giovannetti, P. Khomyakov, G. Brocks, V. v. Karpan, J. Van den Brink, and P. J. Kelly, *Phys. Rev. Lett.* **101**, 026803 (2008).